An Analytical Model of NPS and DQE Comparing Photon Counting and Energy Integrating Detectors

Raymond J. Acciavatti and Andrew D. A. Maidment, Ph.D.
University of Pennsylvania, Department of Radiology, 3400 Spruce St., Philadelphia PA 19104
E-mail: racci@seas.upenn.edu and Andrew.Maidment@uphs.upenn.edu

ABSTRACT

In this work, analytical models of the optical transfer function (OTF), noise power spectra (NPS), and detective quantum efficiency (DQE) are developed for two types of digital x-ray detectors. The two detector types are (1) energy integrating (EI), for which the point spread function (PSF) is interpreted as a weighting function for counting x-rays, and (2) photon counting (PC), for which the PSF is treated as a probability. The OTF is the Fourier transform of the PSF. The two detector types, having the same PSF, possess an equivalent OTF. NPS is the discrete space Fourier transform (DSFT) of the autocovariance of signal intensity. From first principles, it is shown that while covariance is equivalent for both detector types, variance is not. As a consequence, provided the two detector types have equivalent PSFs, a difference in NPS exists such that $NPS_{PC} \geq NPS_{EI}$ and hence $DQE_{PC} \leq DQE_{EI}$. The necessary and sufficient condition for equality is that the PSF is either zero or unity everywhere. A PSF modeled as the convolution of a Lorentzian with a rect function is analyzed in order to illustrate the differences in NPS and DQE. The Lorentzian models the blurring of the x-ray converter, while the rect function reflects the sampling of the detector. The NPS difference between the two detector types is shown to increase with increasing PSF width. In conclusion, this work develops analytical models of OTF, NPS, and DQE for energy integrating and photon counting digital x-ray detectors.

Keywords: Energy integrating detector, photon counting detector, point spread function (PSF), optical transfer function (OTF), modulation transfer function (MTF), noise power spectra (NPS), detective quantum efficiency (DQE).

1. INTRODUCTION

At a broad level, digital x-ray detectors can be divided into two main types, energy integrating and photon counting. An energy integrator detects the sum of the energies of the incident x-rays, while a photon counter detects the presence of individual x-ray quanta as discrete events independent of energy. In this work, we posit the existence of a fundamental difference in imaging performance between these two detector types even in the case of a monoenergetic x-ray beam. As a prerequisite to that analysis, it is helpful to review the physics of the two detector types.

A typical energy integrating detector consists of a scintillator placed in electrical contact with a large area plate of amorphous silicon (*a*-Si). The scintillator converts each incident x-ray to visible light to an intensity proportional to the x-ray energy. Common scintillators include Gd_2O_2S:Tb, a turbid granular phosphor in which light spreads by optical scatter, and CsI:Tl, a structured phosphor in which needle-like crystals approximately 10 μm in diameter channel the light down to the *a*-Si plate by total internal reflection. Although structured phosphors have the drawback of being more expensive to produce, they have the advantage of improved spatial resolution, as they minimize the lateral spread of visible light.[1,2] Ultimately, the visible light is absorbed by photodiodes arranged in a rectangular array within the *a*-Si plate, and is re-emitted as electrons by the photoelectric effect.[3,4,5] The current established by the flow of electrons in the photodiode of each pixel provides the input for an integrating circuit such as the one shown in Figure 1A, so that the readout voltage per pixel is proportional to the sum of the energies of the incident x-rays.

In addition to phosphor-based detectors, amorphous selenium (*a*-Se) photoconductors operated in drift mode have shown promise as energy integrators. This form of energy integrating detector is said to be a direct converter, as the incident x-ray signal generates an image without intermediate conversion of x-rays to visible light. In this detector, an absorbed x-ray ionizes a Se atom located within the thickness of the *a*-Se semiconductor, and creates an electron-hole pair. As a result of an electric field applied normal to the photoconductor surface, the electron and hole migrate in a nearly perfect

orthogonal path to the two different ends of the detector, and an image is formed. A defining characteristic of drift mode is that the electric field is small enough so that the electron moving along the field lines does not have sufficient kinetic energy between collisions to ionize additional Se atoms and hence to create an avalanche formation of electrons and holes. Photoconducting detectors operated in drift mode have superior spatial resolution to phosphor-based detectors. In fact, to a first approximation, the modulation transfer function (MTF) of a-Se operated in drift mode is essentially unity for all spatial frequencies.[6] Although photoconductors and phosphor-based detectors differ in terms of their spatial resolution, they are similar in that they both present the advantage of a large sensitive area and that they both possess the drawbacks of limited dynamic range and sensitivity to dark current and electronic read-out noise.[7]
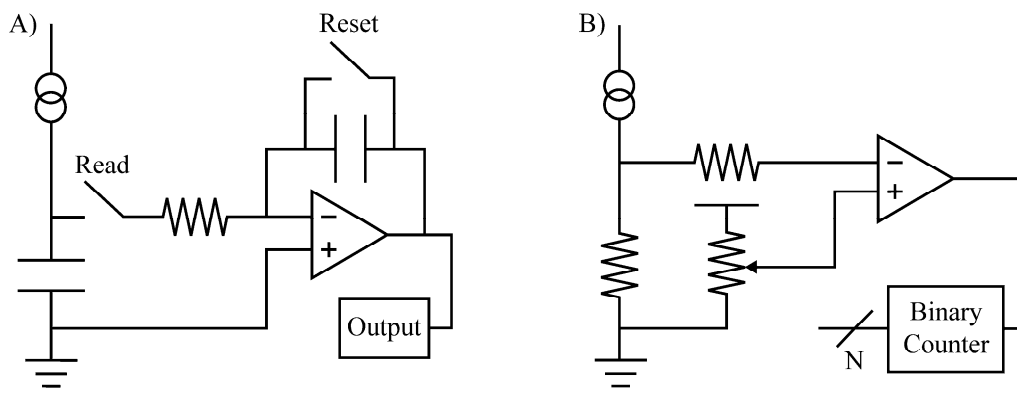

Fig. 1 Shown here are schematic diagrams of the electrical circuits for processing current in the photodiodes of (A) an energy integrating detector and (B) a photon counting detector.

In order to surmount the drawbacks associated with energy integrating detectors, photon counting detectors have been developed. A typical photon counting detector is an avalanche photodiode (APD) placed in electrical contact with an a-Si pixel layer. A common example of an APD is a silicon photomultiplier operated in one of two modes, proportional or Geiger. In proportional mode, the applied electric field is large enough so that a primary electron generated from an x-ray ionization has sufficient energy to ionize additional atoms and to generate an avalanche of electrons and holes. The electrons and holes produced in the avalanche spread laterally, causing blurring in the resultant image. By elevating the bias voltage above breakdown by approximately 10-20%, an APD is converted from proportional mode to Geiger mode. Whereas only an electron can ionize atoms in proportional mode in silicon photomultipliers, both electrons and holes can ionize atoms in Geiger mode.[8] In either proportional or Geiger mode, the voltage gain of the avalanche associated with each pixel is compared against a user-determined threshold established by the potentiometer of a circuit such as the one shown in Figure 1B. Voltage gains exceeding the threshold are counted as representative of one x-ray, and the pixel output is determined by simply summing these counts. The principal advantage of Geiger mode over proportional mode is the production of large, well-defined voltage gains compared against the threshold. This benefit is crucial in applications such as fluoroscopy in which there is low signal compared with the electronic noise level. Additional benefits of Geiger mode are low dark count rate, large dynamic range, and low rate of after-pulsing.[9] Geiger mode does have several drawbacks, however, such as a large recovery time, increased thermal electron generation, and smaller sensitivity area.[10]

In addition to APDs, there has been considerable interest in gaseous detectors as alternative forms of photon counters. In these detectors, each x-ray generates a cascade of ionizations of gas atoms, and voltage gains exceeding a threshold are counted as representative of one x-ray. Since x-rays in the medical imaging energy range of 1 to 50 keV interact with the gas primarily by the photoelectric effect, which increases in prevalence with the atomic number Z of the gas, high Z inert gases such as Kr and Xe are commonly used in these detectors. Increasing the absorption efficiency by using a high Z gas prevents x-rays from propagating large distances before initiating a primary ionization, thereby preventing each x-ray from being attenuated before generating a cascade. To increase absorption efficiency further, the gases are typically placed under high pressure. Finally, to smooth avalanche amplification, which is exponential with the applied electric field, a quencher gas such as CO_2 is often added to the mixture.[11]

One important area of distinction between energy integrating and photon counting detectors, regardless of the specific form of either detector type, is in the weighting of the information carried by individual x-rays in a polyenergetic beam. Energy integrating detectors give the output signal of high energy photons more weight than low energy photons, while photon counting detectors give the output signals equal contribution. As a direct result of this distinction, Tapiovaara and Wagner have shown that a difference in detective quantum efficiency (DQE) arises between the two detector types when they are exposed to broad spectra, polyenergetic x-ray beams. Using the notation of the authors, DQE is calculated for both detector types from the expression

$$\text{DQE} = A \frac{\left[\int \left(\overline{N_1(E)} - \overline{N_2(E)} \right) \eta(E) \psi(E) dE \right]^2}{\int \left(\overline{N_1(E)} + \overline{N_2(E)} \right) \eta(E) \psi^2(E) dE} \ , \tag{1}$$

where $N_i(E)$ is the photon fluence spectra for energy E either in the absence of signal ($i = 1$) or presence of signal ($i = 2$), $\eta(E)$ is the fraction of absorbed x-ray quanta, $\psi(E)$ is the output response of the detector for each incident x-ray, and A is the detector area which is taken to be large compared to the width of the point spread function (PSF). Eq. (1) assumes that the incident x-ray quanta of variable energy E are Poisson-distributed random variables with mean $A\overline{N_i(E)}$, and are detected by a binomial process whose resultant distribution is Poisson with mean $A\overline{N_i(E)}\eta(E)$. The calculation of DQE is different for the two detector types in that the energy integrating detector has the output response $\psi(E) = E$, while the photon counting detector exhibits the output response $\psi(E)$ = constant. Using these two substitutions in Eq. (1), Tapiovaara and Wagner investigated the degradation in DQE as a function of the x-ray tube kilovoltage (kV), assuming the presence of an ideal antiscatter grid, a noiseless detector, and complete x-ray absorption. Raising the kV served the purpose of increasing the width of the polyenergetic x-ray spectra. The authors demonstrated that while both detector types have DQE degradation with increasing kV, the degradation is more considerable as a function of kV for the energy integrating detector than for the photon counting detector. Furthermore, the authors showed that for any fixed kV, the DQE difference between the two detector types is more pronounced in imaging bone and iodine than in imaging soft tissue.[12]

Although Tapiovaara and Wagner characterized the DQE difference between the two detector types in the case of polyenergetic x-rays, their work does not predict DQE differences in the case of monoenergetic x-rays. For this reason, the purpose of this work is to propose analytical models of the optical transfer function (OTF), noise power spectra (NPS), and DQE for energy integrating and photon counting digital x-ray detectors reflecting intrinsic blurring and noise disparities between the two detector types even in the case of monoenergetic x-rays. To that end, we begin by deriving analytical expressions for the signal intensity autocovariance of the two detector types from first principles, and show that these expressions are different for energy integrating and photon counting digital x-ray detectors. The autocovariance analysis facilitates the development of a key theorem regarding the NPS difference between the two detector types. An important corollary of this theorem is then derived as it relates to OTF and DQE. To illustrate OTF, NPS, and DQE calculations for the two detector types, a PSF modeling the blurring of the x-ray converter as a Lorentzian is analyzed. For the purpose of this work, we have limited our focus to a one-dimensional detector as a useful pedagogical tool for illustrating the differences between the two detector types, but we point out that the general methods for computing OTF, NPS, and DQE are readily extended to a two-dimensional detector.

2. METHODS

2.1 Energy Integrating Autocovariance

Suppose that a one-dimensional (1D) energy integrating digital x-ray detector of total length L is centered on the origin and is partitioned into pixels of length l placed end-to-end. We may define the center of each pixel as position X_n, where n is an integer used for unique labeling of the pixels. Each x-ray landing on the detector at position x is counted by each pixel centered at X_n with a weight $w(x - X_n)$ ranging from zero to unity. For the purpose of this work, we will assume that the weighting function for counting x-rays is dependent only upon the displacement of each x-ray from the pixel center, so that it exhibits invariance under translations across pixels. Under these assumptions, the total signal intensity I_n recorded by each pixel centered at X_n is found by summing the weights for counting each incident x-ray

$$I_n = \sum_{m=1}^{N} w(x_m - X_n) \quad , \tag{2}$$

where x_m is the position at which the mth x-ray photon is incident on the detector and where N is the total number of x-rays landing on the detector.

In an ideal energy integrating detector, the weighting function $w(x - X_n)$ should be exactly unity if the x-ray lands within the pixel length and zero if the x-ray lands elsewhere, so that there is no cross-talk between pixels. In a blurring detector, however, an x-ray landing outside of the nth pixel may indeed cause that pixel to record a fractional count. The spatial correlation of pixels can be expressed in terms of the signal intensity autocovariance function, given as

$$K_{nn'} = \left\langle (I_n - \bar{I}_n)(I_{n'} - \bar{I}_{n'}) \right\rangle = \left\langle I_n I_{n'} \right\rangle - \bar{I}_n \bar{I}_{n'} \quad . \tag{3}$$

Defining the x-ray fluence as $\Phi = N/L$ and defining the intensity transfer characteristic G_n of the nth pixel as

$$G_n = \int_{-L/2}^{L/2} w(x - X_n)dx \quad , \tag{4}$$

it follows from Eqs. (2)-(4) that the signal intensity autocovariance is

$$\left\langle (I_n - \bar{I}_n)(I_{n'} - \bar{I}_{n'}) \right\rangle_N = \left\langle \left(\sum_{m=1}^{N} w(x_m - X_n) \right) \left(\sum_{m'=1}^{N} w(x_{m'} - X_{n'}) \right) \right\rangle - \Phi^2 G_n G_{n'} \tag{5}$$

$$= \sum_{m=1}^{N} \sum_{m'=1}^{N} \left\langle w(x_m - X_n)w(x_{m'} - X_{n'}) \right\rangle - \Phi^2 G_n G_{n'} \quad , \tag{6}$$

where the linearity of the expectation operation permits the transition from Eq. (5) to Eq. (6). On the left-hand side of Eq. (5), the subscript N is applied to emphasize that the number of x-rays landing on the detector is precisely known. This condition will be removed shortly. In the double sum of Eq. (6), the N terms for which $m = m'$ and the $N^2 - N$ terms for which $m \neq m'$ can be evaluated separately, giving

$$\left\langle (I_n - \bar{I}_n)(I_{n'} - \bar{I}_{n'}) \right\rangle_N = N\left\langle w(x_m - X_n)w(x_m - X_{n'}) \right\rangle + (N^2 - N)\left\langle w(x_m - X_n) \right\rangle\left\langle w(x_{m'} - X_{n'}) \right\rangle - \Phi^2 G_n G_{n'} \quad . \tag{7}$$

The second term of the expansion in Eq. (7) incorporates the fact that the quantities $w(x_m - X_n)$ and $w(x_{m'} - X_{n'})$ are independent provided $m \neq m'$. Noting that

$$\left\langle w(x_m - X_n) \right\rangle\left\langle w(x_{m'} - X_{n'}) \right\rangle = \int_{-L/2}^{L/2} \frac{dx}{L} w(x - X_n) \int_{-L/2}^{L/2} \frac{dx'}{L} w(x' - X_{n'}) = \frac{G_n G_{n'}}{L^2} \quad , \tag{8}$$

one finds the signal intensity autocovariance to be

$$\left\langle (I_n - \bar{I}_n)(I_{n'} - \bar{I}_{n'}) \right\rangle_N = N\left\langle w(x_m - X_n)w(x_m - X_{n'}) \right\rangle - \frac{\Phi G_n G_{n'}}{L} \quad . \tag{9}$$

The second term in Eq. (9) is negligible in the limit of an infinitely long detector ($L \to \infty$).

In order to generalize Eq. (9) to incorporate the possibility that the number of x-rays landing on the entire detector is not uniform from one experiment to the next but instead exhibits temporal variation, one may assume that N is a Poisson-distributed random variable. To compute the signal intensity autocovariance in this case, begin by noting that

$$\left\langle I_n I_{n'} \right\rangle - \bar{I}_n \bar{I}_{n'} = \left\langle \left\langle (I_n - \bar{I}_n + \bar{I}_n)(I_{n'} - \bar{I}_{n'} + \bar{I}_{n'}) \right\rangle_N \right\rangle - \bar{I}_n \bar{I}_{n'} \quad . \tag{10}$$

The nested brackets emphasize that one can first average for fixed values of N and then average over the varying numbers of incident x-ray quanta. Expanding terms gives

$$\langle I_n I_{n'} \rangle - \bar{I}_n \bar{I}_{n'} = \left\langle \left\langle (I_n - \bar{I}_n)(I_{n'} - \bar{I}_{n'}) \right\rangle_N \right\rangle + \left\langle \left\langle (I_n - \bar{I}_n)\bar{I}_{n'} \right\rangle_N \right\rangle + \left\langle \left\langle \bar{I}_n I_{n'} \right\rangle_N \right\rangle - \bar{I}_n \bar{I}_{n'} \ . \tag{11}$$

Since

$$\left\langle I_n - \bar{I}_n \right\rangle_N = 0 \ , \tag{12}$$

one sees that the second term of the expansion in Eq. (11) vanishes. The third and fourth terms combine as

$$\left\langle \left\langle \bar{I}_n I_{n'} \right\rangle_N \right\rangle - \bar{I}_n \bar{I}_{n'} = \frac{G_n G_{n'}}{L^2} \left[\left\langle N^2 \right\rangle - \left\langle N \right\rangle^2 \right] \ . \tag{13}$$

The assumption that the variance in the number of x-rays is equal to the mean number of x-rays, as would be the case for Poisson statistics,[13] can be introduced into Eq. (13) so that Eq. (11) can be simplified as

$$\langle I_n I_{n'} \rangle - \bar{I}_n \bar{I}_{n'} = \left\langle \left\langle (I_n - \bar{I}_n)(I_{n'} - \bar{I}_{n'}) \right\rangle_N \right\rangle + \frac{\overline{\Phi} G_n G_{n'}}{L} \ . \tag{14}$$

Combining Eq. (14) with Eq. (9) yields the final expression for the signal intensity autocovariance of an energy integrating detector

$$K_{nn'} = \overline{N} \left\langle w(x_m - X_n) w(x_m - X_{n'}) \right\rangle = \overline{\Phi} \int_{-L/2}^{L/2} w(x - X_n) w(x - X_{n'}) dx \tag{15}$$

where $\overline{\Phi} = \overline{N}/L$. This derivation can be easily extended to two dimensions for a 2D detector to yield a similar result.

2.2 Photon Counting Autocovariance

Suppose now that the output of each pixel in detecting an x-ray landing on position x is binary (*i.e.*, either zero or unity), as would be the case for a photon counter. Consequently, instead of being detected by the nth pixel based upon a fractional weight ranging from zero to unity, each incident x-ray is either counted as unity with probability $p(x - X_n)$ or counted as zero with probability $1 - p(x - X_n)$. For the purpose of this work, we will assume that $p(x - X_n)$ is mathematically equivalent to $w(x - X_n)$, although its interpretation is different. Denoting C_n as the total counts of the nth pixel, similar logic up to Eq. (9) holds so that the signal intensity autocovariance can be calculated as

$$\left\langle (C_n - \overline{C}_n)(C_{n'} - \overline{C}_{n'}) \right\rangle_N = N \left\langle Q_n(x_m) Q_{n'}(x_m) \right\rangle - \frac{\Phi G_n G_{n'}}{L} \ , \tag{16}$$

where G_n is the intensity transfer characteristic given by Eq. (4) with the exchange of $w(x - X_n)$ for $p(x - X_n)$, and where the quantity $Q_n(x_m)$ is defined to be unity if the mth x-ray is counted by the nth pixel and zero otherwise. Unlike the energy integrating detector, one must separately consider the cases $n \neq n'$ and $n = n'$ in order to simplify Eq. (16). Beginning with $n \neq n'$, one observes that

$$\left\langle Q_n(x_m) Q_{n'}(x_m) \right\rangle = \int_{-L/2}^{L/2} \frac{dx}{L} p(x - X_n) p(x - X_{n'})(1)(1) + \int_{-L/2}^{L/2} \frac{dx}{L} p(x - X_n)[1 - p(x - X_{n'})](1)(0)$$
$$+ \int_{-L/2}^{L/2} \frac{dx}{L} [1 - p(x - X_n)] p(x - X_{n'})(0)(1) + \int_{-L/2}^{L/2} \frac{dx}{L} [1 - p(x - X_n)][1 - p(x - X_{n'})](0)(0) \tag{17}$$

where the four terms represent the four possible outcomes of the x-ray being counted by the two pixels. Conveniently, the final three terms vanish. The case $n = n'$ is different, however,

$$\left\langle Q_n^2(x_m) \right\rangle = \int_{-L/2}^{L/2} \frac{dx}{L} p(x - X_n)(1^2) + \int_{-L/2}^{L/2} \frac{dx}{L} \left[1 - p(x - X_n)\right](0^2) \qquad (18)$$

for there are only two possible outcomes of the x-ray being counted by a single pixel. Again, only the first term is non-zero. Combining Eqs. (17)-(18) with Eq. (14) to incorporate the assumption that N is a Poisson-distributed random variable, one can write in summary that the signal intensity autocovariance of the photon counting detector is

$$K_{nn'} = \begin{cases} \overline{\Phi} G_n & n = n' \\ \overline{\Phi} \int_{-L/2}^{L/2} p(x - X_n)p(x - X_{n'})dx & n \neq n \end{cases} \qquad (19)$$

One sees that covariance has the same form for both detector types, but variance does not.

2.3 Comparative Analysis of the Two Detector Types

With expressions for the signal intensity autocovariance of the two detector types established, local NPS or Wiener spectra $W(v)$ for pixel n' can now be calculated as the discrete space Fourier transform (DSFT) of the signal intensity autocovariance[14,15]

$$W(v) = l \sum_n K_{nn'} e^{-2\pi i (n - n') l v} \quad , \qquad (20)$$

where v denotes spatial frequency. Assuming that the two detector types have the same point spread function $P(x - X_n)$, which is equivalent to both $w(x - X_n)$ and $p(x - X_n)$, a frequency-independent difference in their NPS may arise from the differing variance

$$W_{PC} - W_{EI} = l(K_{nn}^{PC} - K_{nn}^{EI}) = \overline{\Phi} l \int_{-L/2}^{L/2} \left[P(x - X_{n'}) - P^2(x - X_{n'})\right]dx \quad , \qquad (21)$$

where K_{nn} denotes the variance of either the photon counting detector or the energy integrating detector based on the superscripts. A key theorem can now be written about the NPS difference established by Eq. (21). Namely, the difference vanishes if and only if $P(x - X_{n'}) = P^2(x - X_{n'})$. This property is uniquely satisfied by a binary PSF that is either zero or unity everywhere along the detector. Otherwise, a frequency-independent difference in NPS exists such that $NPS_{PC} > NPS_{EI}$. This result assumes a piece-wise continuous PSF appropriately bounded between zero and unity.

Unlike NPS, the optical transfer function $T(v)$ is equivalent for the two detector types provided that they possess the same PSF, and is calculated as the Fourier transform of the PSF. This property arises immediately from linear response theory for digital x-ray detectors,[16] since the expected output D_n at X_n in response to an input x-ray flux f is given for either detector type as

$$D_n = \int_{-\infty}^{\infty} P(x' - X_n)f(x')dx' \quad . \qquad (22)$$

To verify that the expected output in response to a single x-ray landing at position x is $P(x - X_n)$, as we have assumed repeatedly throughout this work for both detector types, one simply inserts the Dirac delta function $\delta(x' - x)$ as the input flux f in Eq. (22). Now, with the local DQE calculated for both detector types as

$$DQE(v) = \overline{\Phi} \frac{|T(v)|^2}{W(v)} \quad , \qquad (23)$$

it follows that one important corollary of the comparative NPS theorem and the observation that the two detector types possess the same OTF is that DQE may differ between the two detector types in the case where $NPS_{PC} > NPS_{EI}$, so that $DQE_{PC} < DQE_{EI}$. Unlike the NPS difference between the two detector types, the DQE difference is indeed spatial frequency dependent.

3. RESULTS

Local OTF, NPS, and DQE calculations for the two detector types are now illustrated for a pixel in an infinitely long detector ($L \to \infty$) whose PSF is given as the convolution of a Lorentzian with a rect function. The Lorentzian models the blurring of the x-ray converter, while the rect function reflects the sampling of the detector.

$$P(x) = \frac{\Gamma}{2\pi} \frac{1}{x^2 + (\Gamma/2)^2} * \mathrm{rect}\left(\frac{x}{al}\right) = \frac{1}{\pi}\left[\arctan\left(\frac{2x + al}{\Gamma}\right) - \arctan\left(\frac{2x - al}{\Gamma}\right)\right] \tag{24}$$

The Lorentzian has been normalized by area, and its full width at half maximum (FWHM) has been denoted Γ. A Lorentzian has been shown to be a valid approximation for the blurring function of evaporated CsI.[17,18,19] While most photon counting detectors do not use a phosphor as the x-ray converter, the Lorentzian approximation is expected to be relatively independent of technology. The rect function in Eq. (24) is defined to be unity over the length al centered on the origin and zero elsewhere, where a specifies the percentage of the pixel length that is sensitive to the detection of x-rays. With standard properties concerning convolutions, it is straightforward to show that the PSF of Eq. (24) is bounded between zero and unity, as required for application of the comparative NPS theorem.

Assuming that the entire pixel is sensitive to the detection of x-rays, the PSF is plotted versus position in Figure 2A for four values of the FWHM of the blurring function of the x-ray converter. Unless otherwise indicated, all subsequent figures also make the assumption that $a = 1$. Figure 2A illustrates that increasing Γ increases the spread of the tails of the PSF and reduces the width of its plateau. To calculate the OTF associated with the PSF of Eq. (24), one may apply the convolution theorem to obtain

$$T(\nu) = G e^{-\pi\Gamma|\nu|}\mathrm{sinc}(al\nu) \quad , \quad \mathrm{sinc}(z) \equiv \frac{\sin(\pi z)}{\pi z} \quad , \quad G \equiv al \tag{25}$$

where G is the intensity transfer characteristic. The normalized modulus of the OTF gives the MTF, which is plotted versus spatial frequency in Figure 2B. Increasing Γ decreases the MTF at all spatial frequencies and hence worsens spatial resolution.
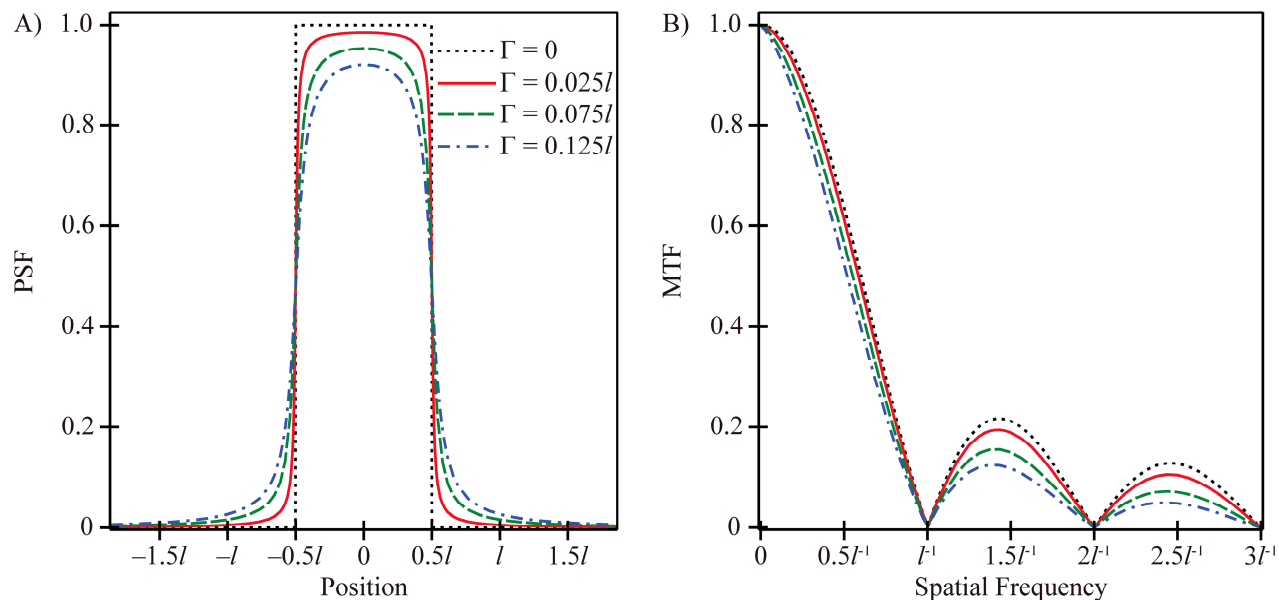

Fig. 2 (A) The PSF is plotted versus position in increments of pixel length (l) for four different FWHMs (Γ) of the Lorentzian x-ray converter blurring function, assuming that the entire pixel is sensitive to the detection of x-rays ($a = 1$). Increasing Γ reduces the width of the plateau of the PSF and increases the spread of its tails. (B) The MTF is plotted versus spatial frequency, illustrating that increasing Γ worsens resolution. The two subfigures share a common legend.

A comparative analysis of the NPS of the two detector types can now be performed. Since the PSF is symmetric about the center of the pixel, NPS_{EI} is determined from the expression

$$W_{\text{EI}}(\nu) = l \sum_{n=-\infty}^{\infty} K_{n,0}^{\text{EI}} \cos(2\pi n l \nu) \quad , \quad K_{n,0}^{\text{EI}} = \overline{\Phi} \int_{-\infty}^{\infty} |T(\nu)|^2 \, e^{-2\pi i n l \nu} d\nu \tag{26}$$

where the integral for calculating the energy integrating signal intensity autocovariance as given by Eq. (15) has been rewritten in Fourier space using Parseval's theorem.[20] Using Eq. (25) for $T(\nu)$, the autocovariance integral of Eq. (26) can be evaluated with the help of a computer algebra system (CAS).

$$K_{n,0}^{\text{EI}} = \frac{\overline{\Phi}}{\pi} \left[\begin{array}{c} \Gamma \ln\left(\dfrac{\Gamma^2 + n^2 l^2}{\sqrt{\left(\Gamma^2 + (n+a)^2 l^2\right)\left(\Gamma^2 + (n-a)^2 l^2\right)}} \right) + (n+a)l \arctan\left(\dfrac{(n+a)l}{\Gamma} \right) \\ \\ + (n-a)l \arctan\left(\dfrac{(n-a)l}{\Gamma} \right) - 2nl \arctan\left(\dfrac{nl}{\Gamma} \right) \end{array} \right] \tag{27}$$

To determine NPS_{PC}, one simply adds to Eq. (26) the frequency-independent NPS difference

$$W_{\text{PC}} - W_{\text{EI}} = \overline{\Phi} l^2 \left[a - \frac{\Gamma}{\pi l} \ln\left(\frac{\Gamma^2}{\Gamma^2 + a^2 l^2} \right) - \frac{2a}{\pi} \arctan\left(\frac{al}{\Gamma} \right) \right]. \tag{28}$$

The NPS difference is determined from Eq. (21) based on the differing variances of the two detector types. Whereas the variance of the energy integrator is the $n = 0$ component of Eq. (27), the variance of the photon counter is $\overline{\Phi} G$, where G is the intensity transfer characteristic as stated in Eq. (25).

In Figure 3A, the variances of the two detector types are plotted versus Γ for three pixel sensitivity lengths. Figure 3A shows that the variance of the photon counter is independent of the blurring of the x-ray converter, while the variance of the energy integrator is reduced with increased blurring, tending to zero in the limit of infinite blurring. For either detector type, lowering the pixel sensitivity length reduces the variance. In the limit of an optimally-resolving x-ray converter ($\Gamma = 0$), the variances of the two detector types match, making the NPS difference vanish. In Figure 3B, plots of NPS_{EI} and NPS_{PC} versus spatial frequency are shown. Figure 3B demonstrates that in a blurring detector, the photon counter is noisier than the energy integrator, where NPS_{PC} is found by adding the white noise of Eq. (28) to NPS_{EI}. In the limit of a perfectly-resolving x-ray converter, the two detector types possess the same white NPS.

To illustrate that the NPS difference between the two detector types increases with the blurring of the x-ray converter, the NPS difference is plotted versus Γ in Figure 3C. In the limiting case of infinite blurring in the x-ray converter, the NPS difference plateaus to its maximum.

$$\lim_{\Gamma \to \infty} (W_{\text{PC}} - W_{\text{EI}}) = a\overline{\Phi} l^2 \tag{29}$$

Infinite blurring in the x-ray converter gives rise to a non-imaging system which simply detects the number of incident x-ray quanta without distinguishing their position along the detector. An additional property seen in Figure 3C is that decreasing the pixel sensitivity length reduces the NPS difference. Using Eq. (23) and the preceding NPS results, DQE is plotted versus frequency in Figure 3D. Figure 3D demonstrates that DQE_{PC} is inferior to DQE_{EI} at all frequencies, except in the limiting case of a perfectly-resolving x-ray converter for which the DQEs of both detector types match.

$$\lim_{\Gamma \to 0} \text{DQE}(\nu) = a \cdot \text{sinc}^2(al\nu) \tag{30}$$

Figure 3D indicates that DQE_{EI} increases with the blurring of the x-ray converter while DQE_{PC} decreases with the blurring of the x-ray converter.
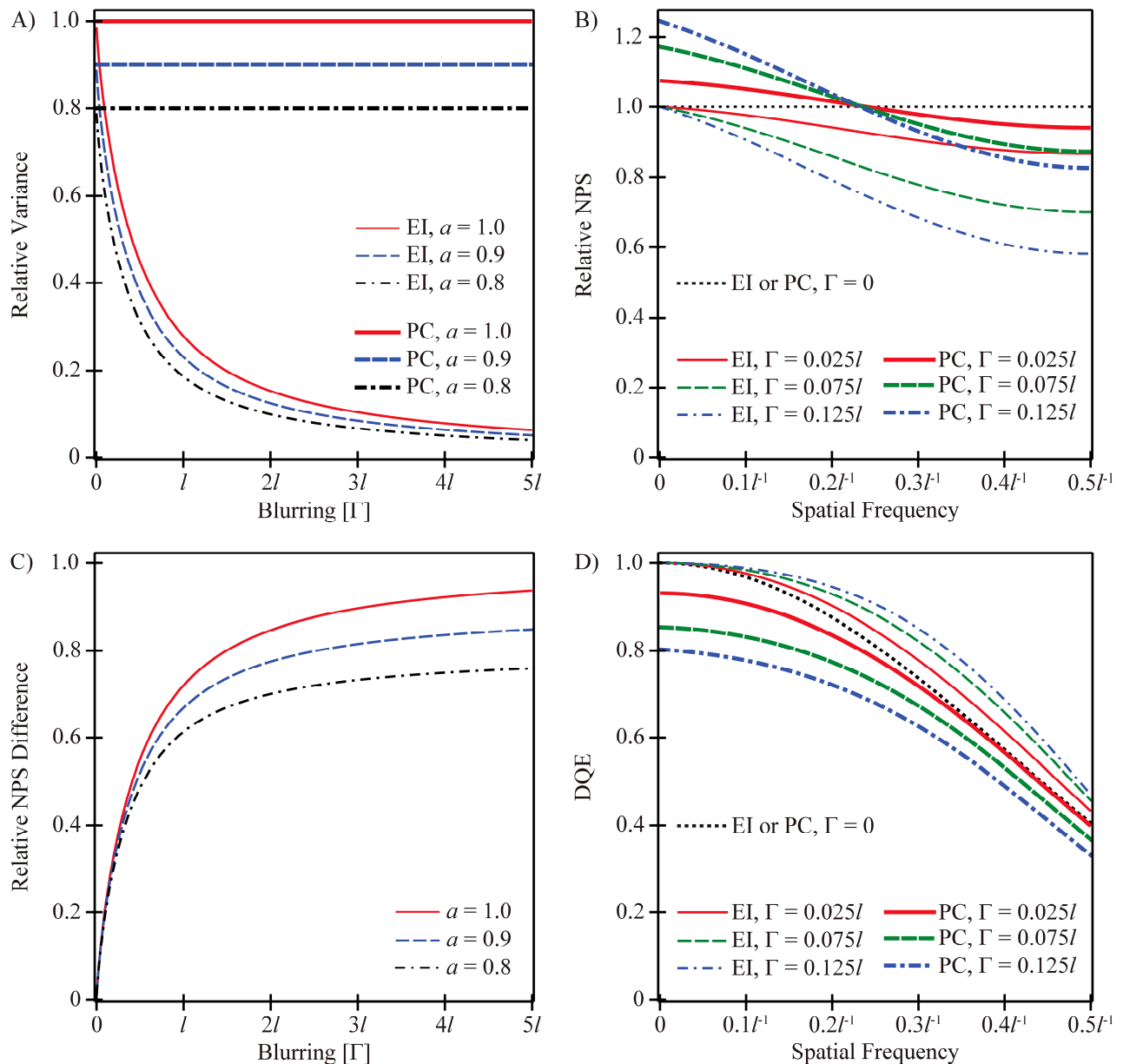
Fig. 3 (A) The variance of the two detector types is plotted versus Γ for three pixel sensitivity lengths. (B) The relative NPS is plotted versus spatial frequency assuming that the entire pixel is sensitive to the detection of x-rays. (C) The NPS difference between the two detector types is shown to increase with increasing PSF width. (D) The DQE is plotted versus spatial frequency for the two detector types assuming that the entire pixel is sensitive to the detection of x-rays.

The dependence of the DQE on the blurring of the x-ray converter is studied explicitly in Figure 4A in the special case of $v = 0$. Figure 4A shows that DQE(0) is the same for the two detector types in the limit of a perfectly-resolving x-ray converter and is equivalent to a, the percentage of the pixel length that is sensitive to the detection of x-rays. However, once the FWHM of the Lorentzian increases from zero, the behavior of DQE(0) is quite different for the two detector types. $DQE_{EI}(0)$ is unity for all blurring profiles of the x-ray converter if the entire pixel is sensitive to the detection of x-rays, and increases with the blurring of the x-ray converter to unity in the limit of a non-imaging detector if only a portion of the pixel is sensitive to x-rays. By contrast, $DQE_{PC}(0)$ decreases with the blurring of the x-ray converter for all pixel sensitivity lengths and in the limit of a non-imaging detector attains a different horizontal asymptote

$$\lim_{\Gamma \to \infty} \text{DQE}_{PC}(0) = \frac{a}{1+a} \quad . \tag{31}$$

With a = 1.0, 0.9, and 0.8 as used in Figure 4A, the horizontal asymptotes from Eq. (31) are $1/2 = 0.5$, $9/19 \approx 0.474$, and $4/9 \approx 0.444$, respectively. As a final point of analysis, Figure 4B illustrates that unlike the difference in NPS between the two detector types, the difference in DQE is indeed spatial frequency dependent. Like the NPS difference, the DQE difference increases with the blurring of the x-ray converter.
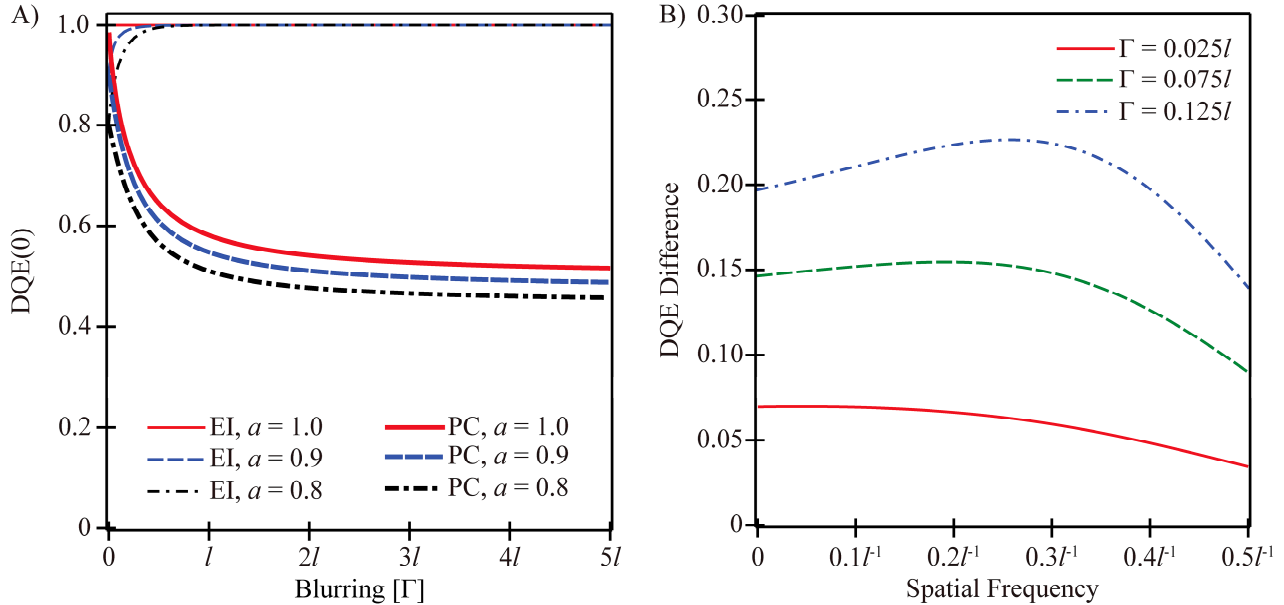
Fig. 4 (A) For both detector types, DQE(0) is plotted versus Γ for three pixel sensitivity lengths. (B) The DQE difference between the two detector types is spatial frequency dependent and increases with the blurring of the x-ray converter. This subplot implicitly assumes that the entire pixel is sensitive to the detection of x-rays.

4. DISCUSSION

This work develops analytical models of OTF, NPS, and DQE for two types of digital x-ray detectors, energy integrating and photon counting. From first principles, we have shown that while OTF is equivalent for two detector types possessing the same PSF, NPS and DQE are not. In particular, we have demonstrated that as a result of differing variance between the two detector types, a frequency-independent difference in NPS exists such that $\text{NPS}_{PC} \geq \text{NPS}_{EI}$ and hence $\text{DQE}_{PC} \leq \text{DQE}_{EI}$. The necessary and sufficient condition for equality is that the PSF is either zero or unity everywhere along the detector. The NPS and DQE inequalities derived in this work imply a benefit associated with energy integrating detectors over photon counting detectors which has not been previously explored in the literature.

The OTF, NPS, and DQE calculations for the two detector types have been illustrated for a model detector whose PSF is the convolution of a Lorentzian with a rect function. The Lorentzian reflects the blurring of the x-ray converter, while the rect function models the sampling of the detector. For the purpose of this example, we assumed that the pixel sensitivity was symmetric about its center. Using the Fourier shift theorem, it can be readily shown that MTF, NPS, and DQE for both detector types are unaffected by a translational shift in the sensitivity length, assuming that this shift is uniform across all pixels.

In the model detector section of this work, it was observed that if the x-ray converter exhibits no blurring, the NPS difference between the two detector types vanishes. We now give a physical argument for the validity of this result as a complement to the mathematical one used in the proof of the comparative NPS theorem. To a good approximation, an x-ray converter with optimal spatial resolution is found in an energy integrating photoconducting detector such as a-Se operated in drift mode. This form of an energy integrating detector can be viewed as the limiting case of a photon

counting silicon photomultiplier with such a small applied electric field that the primary electron generated from an x-ray ionization does not have sufficient energy to create an avalanche of electrons and holes which spread laterally, and hence travels in a near perfect orthogonal path to the *a*-Si pixel layer in forming the image. With no avalanche in either detector type, there is no physical difference in x-ray detection between the photon counter and the energy integrator when both are exposed to a monoenergetic x-ray beam. Consequently, the two detector types are indeed expected to have identical physical properties such as NPS.

A potential shortcoming of this work is that we have neglected to model a number of factors that could impact detector performance in real imaging systems. For example, energy integrating detectors exhibit increased sensitivity to electronic read-out noise and dark current when compared against photon counting detectors, elevating NPS_{EI} and degrading DQE_{EI}. In addition, in a phosphor-based detector, DQE_{EI} may be reduced due to stochastic variation in the number of optical quanta and in the number of photoelectrons generated for each incident x-ray, as well as imperfect absorption efficiency by the scintillator and the *a*-Si pixel layer.[21] The OTF, NPS, and DQE calculations can also be affected by differing x-ray interactions at each depth of the phosphor. In the model detector section of this work, we have observed that if the entire pixel is sensitive to x-rays, $DQE_{EI}(0)$ is unity regardless of the blurring of the x-ray converter (Figure 4A). However, based on classic observations by Swank and Lubberts, the presence of different x-ray interactions at each depth of a phosphor may lower $DQE_{EI}(0)$ from unity.[22,23] We also have not modeled the effect of the x-ray focal spot size or x-ray parallax which degrades high-frequency information present in the incident x-ray signal. As a final note, we point out that this work has not modeled anti-coincidence logic, designed to suppress cross-talk in a photon counter if multiple pixels fire simultaneously due to a single x-ray input. Since all of these factors have considerable variation over different imaging systems, we find it appropriate to omit an analysis of each one from this work. In experimental practice, they should be modeled on a case-by-case basis for each detector under consideration.

In the model detector section of this work, it was assumed that each pixel is homogeneously sensitive to the detection of x-rays over the length *al*. Under this assumption, we have neglected to consider the lateral diffusion of photoelectrons to neighboring wells within the *a*-Si pixel layer. If one were to incorporate this effect rigorously into the analysis, the rect function of the PSF convolution in Eq. (24) should be replaced with a trapezoid based on the research of Schumann and Lomheim.[24] Schumann and Lomheim have shown that lateral diffusion of photoelectrons is considerable when dealing with long wavelengths (> 800 nm) of infrared light incident on the *a*-Si pixel layer. However, they have demonstrated that lateral diffusion is negligible when shorter wavelengths of visible light land on the pixel layer, such as the wavelengths generated by CsI:Tl in typical imaging systems. It is for this reason that we have omitted Schumann and Lomheim's correction in the model detector section of this work. The wavelength dependence of their correction arises from the fact that silicon is a poor absorber of long wavelengths and a strong absorber of short wavelengths; significant lateral diffusion can only occur in the presence of weak absorption.[25]

5. CONCLUSION

This work develops models of OTF, NPS, and DQE for two types of digital x-ray detectors, energy integrating and photon counting. From first principles, we have shown that although two detector types possessing the same PSF have the same OTF, a frequency-independent NPS difference exists such that $NPS_{PC} \geq NPS_{EI}$. As a result of this property, it follows that $DQE_{PC} \leq DQE_{EI}$. We anticipate that the fundamental techniques for calculating OTF, NPS, and DQE for both detector types, as established by this work, can be extended into many future applications. These applications range from a study of detector edge effects on the NPS difference to an analysis of the impact of projection angle and PSF asymmetry on that difference. In addition, we project that the analytical OTF, NPS, and DQE expressions of this work can be readily adapted to Monte Carlo simulations modeling detectors whose PSFs cannot be written in closed form due to scatter and glare effects or due to complicated dependence on x-ray beam energy.

ACKNOWLEDGEMENT

REFERENCES

[1] E. Samei, "Image quality in two phosphor-based flat panel digital radiographic detectors," Med. Phys. **30**(7), 1747-1757 (2003).

[2] J. A. Rowlands and J. Yorkston, in *Handbook of Medical Imaging*, edited by J. Beutel, H. L. Kundel, and R. L. van Metter (SPIE, Bellingham, WA, 2000), Vol. 1, Chap. 4.

[3] T. Jing, C. A. Goodman, J. Drewery, G. Cho, W. S. Hong, H. Lee, S. N. Kaplan, A. Mireshghi, V. Perez-Mendez, and D. Wildermuth, "Amorphous silicon pixel layers with cesium iodide converters for medical radiography," IEEE Trans. Nucl. Sci. **41**(4), 903-909 (1994).

[4] A. Cowen, S. Kengyelics, and A. Davies, "Solid-state, flat-panel, digital radiography detectors and their physical imaging characteristics," Clin. Radiol. **63**(5), 487-498 (2008).

[5] V. V. Nagarkar, T. K. Gupta, S. R. Miller, Y. Klugerman, M. R. Squillante, and G. Entine, "Structured CsI(Tl) scintillators for x-ray imaging applications," IEEE Trans. Nucl. Sci. **45**(3), 492-496 (1998).

[6] D. L. Lee, L. K. Cheung, B. Rodricks, and G. F. Powell, "Improved imaging performance of a 14 x 17-inch Direct Radiography (TM) System using Se/TFT detector," in *SPIE Conference on Physics of Medical Imaging* [Proc. SPIE **3336**, 14-23 (1998)].

[7] P. M. Fralicciardi, J. Jakubek, D. Vavrik, and J. Dammer, "Comparison of single-photon counting and charge-integrating detectors for X-ray high-resolution imaging of small biological objects," Nuclear Instruments and Methods in Physics Research Section A **607**(1), 221-222 (2009).

[8] G. Lutz, *Semiconductor Radiation Detectors* (Springer, Berlin, 1999).

[9] H. Dautet, P. Deschamps, B. Dion, A. D. MacGregor, D. MacSween, R. J. McIntyre, C. Trottier, and P. P. Webb, "Photon counting techniques with silicon avalanche photodiodes," Applied Optics **32**(21), 3894-3900 (1993).

[10] N. Otte, "The Silicon Photomultiplier – A new device for High Energy Physics, Astroparticle Physics, Industrial and Medical Applications," SNIC Symposium, Stanford, California, 2006.

[11] L. Shekhtman, "Novel position-sensitive gaseous detectors for x-ray imaging," Nuclear Instruments and Methods in Physics Research Section A **522**(1-2), 85-92 (2004).

[12] M. J. Tapiovaara and R. F. Wagner, "SNR and DQE analysis of broad spectrum x-ray imaging," Phys. Med. Biol. **30**(6), 519-529 (1985).

[13] H. H. Barrett and K. J. Myers, *Foundations of Image Science* (Wiley, Hoboken, NJ, 2004).

[14] J. C. Dainty and R. Shaw, *Image Science* (Academic, New York, 1974).

[15] M. L. Giger, K. Doi, and C. E. Metz, "Investigation of basic imaging properties in digital radiography. 2. Noise Wiener spectrum," Med. Phys. **11**(6), 797-805 (1984).

[16] M. Albert and A. D. A. Maidment, "Linear response theory for detectors consisting of discrete arrays," Med. Phys. **27**(10), 2417-2434 (2000).

[17] J.-P. Moy, "Image quality of scintillator-based x-ray electronic imagers," in *SPIE Conference on Physics of Medical Imaging* [Proc. SPIE **3336**, 187-194 (1998)].

[18] C. Chaussat, J. Chabbal, T. Ducourant, V. Spinnler, G. Vieux, and R. Neyret, "New CsI/a-Si 17'' x 17'' x-ray flat-panel detector provides superior detectivity and immediate direct digital output for general radiography systems," in *SPIE Conference on Physics of Medical Imaging* [Proc. SPIE **3336**, 45-56 (1998)].

[19] J.-P. Moy, "Signal-to-noise ratio and spatial resolution in x-ray electronic imagers: Is the MTF a relevant parameter?," Med. Phys. **27**(1), 86-93 (2000).

[20] S. M. Lea, *Mathematics for Physicists* (Brooks/Cole, Belmont, CA, 2004).

[21] M. Rabbani, R. Shaw, and R. Van Metter, "Detective quantum efficiency of imaging systems with amplifying and scattering mechanisms," J. Opt. Soc. Am. A **4**(5), 895–901 (1987).

[22] G. Lubberts, "Random noise produced by x-ray fluorescent screens," J. Opt. Soc. Am. **58**(11), 1475-1483 (1968).

[23] R. K. Swank, "Absorption and noise in x-ray phosphors," J. Appl. Phys. **44**(9), 4199-4203 (1973).

[24] L. W. Schumann and T. S. Lomheim, "Modulation transfer function and quantum efficiency correlation at long wavelengths (greater than 800 nm) in linear charge coupled imagers," Applied Optics **28**(9), 1701-1709 (1989).

[25] G. C. Holst, *CCD Arrays Cameras and Displays*, 2nd ed. (JCD, Winter Park, FL and SPIE, Bellingham, WA, 1998).